Icarus 211 (2011) 1284–1293

Contents lists available at ScienceDirect

Icarus

journal homepage: www.elsevier.com/locate/icarus

Emergence of polar-jet polygons from jet instabilities in a Saturn model

Raúl Morales-Juberías [a,*], Kunio M. Sayanagi [b], Timothy E. Dowling [c], Andrew P. Ingersoll [b]

[a] New Mexico Institute of Mining and Technology, Socorro, NM 87801, USA
[b] California Institute of Technology, Pasadena, CA 91125, USA
[c] University of Louisville, Louisville, KY 40292, USA

ARTICLE INFO

Article history:
Received 23 April 2010
Revised 2 November 2010
Accepted 4 November 2010
Available online 17 November 2010

Keywords:
Jovian planets
Saturn, Atmosphere
Atmospheres, Dynamics

ABSTRACT

Voyager flybys of Saturn in 1980–1981 revealed a circumpolar wave at ≈78° north planetographic latitude. The feature had a dominant wavenumber 6 mode, and has been termed the Hexagon from its geometric appearance in polar-projected mosaics. It was also noted for being stationary with respect to Saturn's Kilometric Radiation (SKR) rotation rate. The Hexagon has persisted for over 30 years since the Voyager observations until now. It has been observed from ground based telescopes, Hubble Space Telescope and multiple instruments onboard Cassini in orbit around Saturn. Measurements of cloud motions in the region reveal the presence of a jet stream whose path closely follows the Hexagon's outline. Why the jet stream takes the characteristic six-sided shape and how it is stably maintained across multiple saturnian seasons are yet to be explained. We present numerical simulations of the 78.3°N jet using the Explicit Planetary Isentropic-Coordinate (EPIC) model and demonstrate that a stable hexagonal structure can emerge without forcing when dynamic instabilities in the zonal jet nonlinearly equilibrate. For a given amplitude of the jet, the dominant zonal wavenumber is most strongly dependent on the peak curvature of the jet, i.e., the second north–south spatial derivative of the zonal wind profile at the center of the jet. The stable polygonal shape of the jet in our simulations is formed by a vortex street with cyclonic and anticyclonic vortices lining up towards the polar and equatorial side of the jet, respectively. Our result is analogous to laboratory experiments of fluid motions in rotating tanks that develop polygonal flows out of vortex streets. However, our results also show that a vortex street model of the Hexagon cannot reproduce the observed propagation speed unless the zonal jet's speed is modified beyond the uncertainties in the observed zonal wind speed, which suggests that a vortex street model of the Hexagon and the observed zonal wind profile may not be mutually compatible.

1. Introduction

Voyager observations of Saturn's northern high latitudes in visible wavelengths revealed the existence of a hexagonal wave encircling the pole at ≈78°N that was termed the Hexagon due to its geometric appearance in polar-projected mosaics (Godfrey, 1988, latitudes are planetographic unless otherwise noted). The Hexagon was stationary within measurement error (0.8 ± 1.1 m s^{-1}) with respect to the radio rotation period of the planet, measured to be 10 h 39 m 22.4 s, which corresponds to a rotation rate $\Omega_{III} = 1.6378 \pm 3 \times 10^{-4}$ s^{-1} (Desch and Kaiser, 1981). The latitudinal width of the clouds associated with the Hexagon was measured to be about 4° relative to the center of the sharp eastward jet located at that latitude. The jet itself had a peak speed of 100 m s^{-1}, as determined from tracking individual cloud patterns that form the Hexagon. The Voyager images also showed a large anticyclonic vortex (diameter ≈ 6000 km) in the anticyclonic shear region directly equatorward of the jet. This spot was also stationary with respect to the radio rotation period of the planet, and it seemed to impinge on the Hexagon flow, and thus a causal relationship between the vortex and the Hexagon was proposed (Allison et al., 1990). Hubble Space Telescope (HST) and ground based observations of the northern hemisphere of Saturn, obtained a decade later between 1990 and 1991, revealed the persistent nature of these two features (Caldwell et al., 1993; Sanchez-Lavega et al., 1993). In these observations, only the spot showed high contrast and reflectivity in the images taken using methane band filters (725, 889 and 899 nm), indicating that the clouds associated with the spot reached higher into the atmosphere than those of the Hexagon. From the comparison between the longitudinal drift rates of the spot measured in the Voyager images versus those measured in the ground based images, Sanchez-Lavega et al. (1993) suggested that the spot observed in 1990 could be different to the one observed in the Voyager era and that changes in their brightness could make them visible at different times. Such change

* Corresponding author. Address: New Mexico Institute of Mining and Technology, Physics Department and Geophysical Research Center, Workman #345, 801 Leroy Place, Socorro, NM 87801, USA. Fax: +1 575 835 5707.
E-mail address: mjuberias@gmail.com (R. Morales-Juberías).

0019-1035/$ - see front matter © 2010 Elsevier Inc. All rights reserved.
doi:10.1016/j.icarus.2010.11.006

in brightness could be due to a change in the properties of the clouds associated with the spot between 1980 and 1990, as suggested by the observed change in the contrast of the spot in different visible filters between the Voyager and ground based observations. In 2006, the Visual Infrared Mapping Spectrometer (VIMS) onboard the Cassini spacecraft obtained new images of the Hexagon at 5 μm (Baines et al., 2009), and in 2009 the Imaging Science Subsystem (ISS) captured its first images of the Hexagon in visible light (Sayanagi et al., 2009). These new observations show that the Hexagon is a long-lived feature that survives Saturn's seasonal changes, and do not provide any evidence of the existence of a spot similar to the one observed in 1980 or 1990, which suggest that such a spot could have been a by-product of the Hexagon, or simply an independent feature, rather than its cause (Fig. 1).

The nature of the Hexagon is largely unknown. Allison et al. (1990) interpreted this feature as a stationary Rossby wave perturbed by an anticyclonic vortex to the south of the eastward jet. From the similarity between the characteristic width of the jet and the wavelength of the wavenumber 6 mode, they also proposed that the same mechanism might be responsible for both the formation of the ≈78°N jet and its hexagonal shape. Several laboratory experiments have shown how vortex streets can shape polygonal flows in fluids in a rotating tank for a wide range of parameters and as a result of different kinds of forcing (Sommeria et al., 1989; Vatistas, 1990; Vatistas et al., 1994; Marcus and Lee, 1998; Jansson et al., 2006). More recently, Barbosa-Aguiar et al. (2010) have shown how the zonal flow around the latitude of the north polar Hexagon is unstable according to linear barotropic theory. They also have shown how polygonal structures, corresponding to wave modes caused by the nonlinear equilibration of barotropically unstable zonal jets, can appear in laboratory experiments of flows in rotating tanks. The polygonal flow in their experiments also appears to be associated with a vortex street.

Here, we present the results of numerical simulations without forcing that show how polygonal patterns can be shaped by a vortex street that emerge when shear instabilities equilibrate in an eastward Gaussian jet placed at the latitude of the Hexagon. The expression "vortex street" is used in this paper to describe staggered vortices of opposite signs with a meandering jet in between them (Humphreys and Marcus, 2007). For an eastward jet, the counterclockwise vortices are slightly to the north of the clockwise vortices. Our results show that, for a jet of a given amplitude, the prevailing factor that controls the dominant zonal wavenumber is the jet's curvature (i.e., second spatial derivative of the zonal wind profile at the center of the jet). In addition, we show how westward flows at the flanks of the eastward jet can slow the propagation rate of the polygons to make them rotate closer to the rate observed for the Hexagon in the Voyager System III rotation rate.

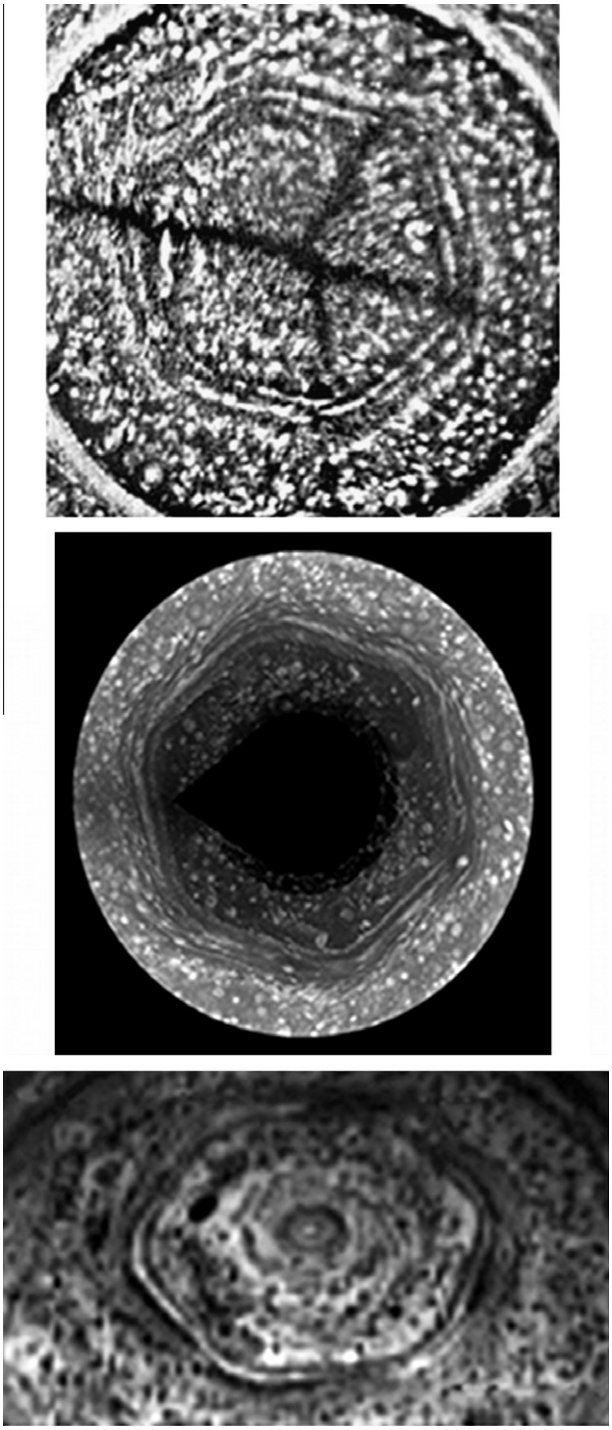

Fig. 1. Hexagon observations from Voyager (Godfrey, 1988, -top-), Cassini-ISS (Sayanagi et al., 2009, -middle-), and Cassini-VIMS (Baines et al., 2009, -bottom-).

2. Simulations

2.1. Model description

The model used in this study is the Explicit Planetary Isentropic-Coordinate (EPIC), General Circulation Model developed by Dowling et al. (1998). The nominal domain consists of a channel that covers 360° in the zonal direction and that extends from 67.3° to 87.3° in the meridional direction, with a resolution of ≈350 × 350 km, corresponding to a grid of 256 × 64 points. Assuming neutral stability according to Arnol'd's second criterion, Dowling and Read (2010) estimates that the dominant deformation radius for the jet at this latitude is $L_d \approx 1135$ km, which is adequately resolved by our simulations. In the vertical direction, the model has 20 layers equally spaced in log(P) that extend from 0.1 mb to 10 bars, with the four top layers set as a damper of vertically propagating waves (i.e., the "sponge" layers). The gravitational acceleration is set to the value corresponding to the latitudinal position of the center of the jet, which is $g(\varphi_0) = 12.14\ \mathrm{m\ s^{-2}}$, for $\varphi_0 = 78.3°$. A high latitude filter is applied poleward of 85°, and a high-order viscosity term ($\nu_6 = 1.76 \times 10^{26}\ \mathrm{m^6\ s^{-1}}$) is used to damp computational modes (Dowling et al., 1998). The time scale for energy removal due to this computational hyper-viscosity can be estimated as $\Delta t \approx (\Delta x)^6\ \nu_6^{-1}$ which for a length scale of $\Delta x \approx 1000$ km is of the order of $\Delta t \approx 10^9$ s (~65×10^3 Earth days).

Our simulations adopt vertical thermal structure that resembles the observed temperature as a function of pressure in the

stratosphere above the 150 mbar level (Tyler et al., 1982), and continuously approaches a constant target value of the Brunt-Väisälä frequency N below that level. As shown in Fig. 2, these synthetic temperature profiles are constructed such that not only the temperature, but also N, is continuous in the vertical.

Following Allison et al. (1990) the shape of the jet used to initialize our first simulations is a Gaussian profile defined as:

$$U(\varphi) = U_0 \exp(-b\gamma^2(\varphi)/2U_0) \quad (1)$$

where U_0 is the peak velocity or amplitude of the jet, b is the peak latitudinal curvature of the jet, φ is the planetographic latitude, $\gamma(\varphi) = \int_{\varphi_0}^{\varphi} R(\varphi')d\varphi'$ is the meridional distance from the center of the jet, and $R(\varphi)$ is the latitudinal map factors in oblate spherical coordinates,

$$R(\varphi) = \frac{R_p^2 R_e^2}{\left[R_p^2 \sin^2(\varphi) + R_e^2 \cos^2(\varphi)\right]^{3/2}} \quad (2)$$

where R_e = 60,330 km and R_p = 54,180 km are the equatorial and polar radius of Saturn respectively. Once the background atmosphere is initialized with a specific vertical thermal profile and a specific zonal wind profile, the model velocity field is seeded with small amplitude noise (≈1 m s^{-1}) to break the symmetry of the wind profile, and the model is then left to evolve without forcing from this barotropic initial condition.

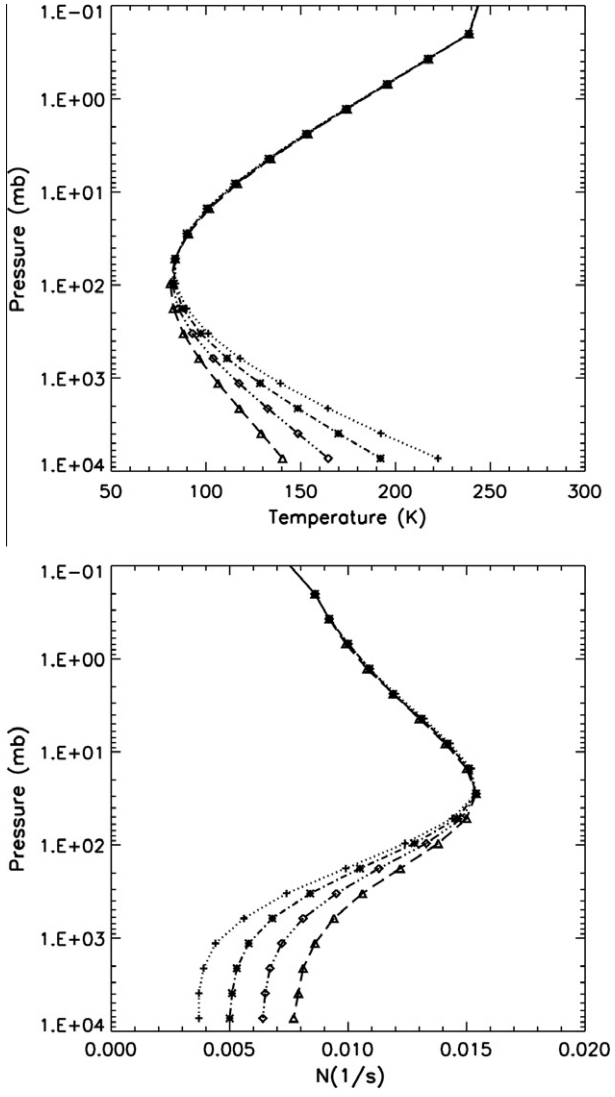

Fig. 2. Thermal profiles used in the simulations described in the paper corresponding to values of N at the bottom of the model of 0.004, 0.005, 0.006, and 0.007 s^{-1}. The symbols on each line represent the location of the layers of the model.

2.2. Polygon formation

Table 1 summarizes our simulations' results, which show that a polygonal structure with a different dominant zonal wavenumber emerges depending on the initial jet parameters U_0 and b. Fig. 3 shows the polar projected maps of potential vorticity corresponding to the simulations initialized with a Gaussian wind with U_0 = 125 m s^{-1} and different values of the curvature parameter b. For the case with $b = 50 \times 10^{-11}$ m^{-1} s^{-1} (U125b050N4) the model equilibrates into a vortex street with a dominant zonal wavenumber of six, and thus the polar projected maps reveal a hexagonal pattern. This hexagonal pattern emerges after ≈45 days of simulated time (unless otherwise noted, 1 day = 24 h), and it persists until the end of the 600 days simulation. Fig. 4 shows the longitudinal average of the zonal wind profile and of the potential vorticity at ≈1500 mb after 300 days for the same simulations shown in Fig. 3. Fig. 4 demonstrates that the equilibrated wind profile continues to have reversals in the zonal mean PV profiles, which represents a violation of Charney-Stern stability criterion. Fig. 5 shows the relationship between the meridional gradient of the zonal mean quasi-gesotrophic potential vorticity ($\overline{Q}_y$, defined as in Lebeau and Dowling, 1998) and the mean zonal wind profile ($\bar{u}$) for the initial condition (left) and for day 300 (right) corresponding to the simulations shown in Fig. 3. The evolution of the meridional gradient of the quasi-gesotrophic potential vorticity with time shows that the flow in our simulations approaches neutral stability according to Arnol'd's second stability criterion (Dowling, 1995).

Fig. 6 shows that all the polygons formed from a Gaussian jet (Table 1) propagate following a Rossby wave dispersion relationship of the form:

$$c = u - \frac{Q_y}{k_x^2 + k_y^2 + k_d^2} \quad (3)$$

where u and Q_y are respectively the zonal velocity and the meridional gradient of the quasi-gesotrophic potential vorticity in the center of the jet, and k_x and k_y are the zonal and meridional wavenumbers respectively, $k_d \equiv 1/L_d$, with the deformation radius L_d = 1135.31 km for the center of the jet (Dowling and Read, 2010). We calculate the zonal wavenumber as $k_x = 2\pi/\lambda_x$, where $\lambda_x = 2\pi r(\varphi_0)/n$, with n being the dominant planetary wavenumber of the polygon (e.g, Hexagon is n = 6), and $r(\varphi)$ the longitudinal map factor in oblate spherical coordinates,

Table 1
Results of the simulations initialized with zonal winds described by Eq. (1), and a thermal stratification in the bottom of the model of N = 0.004 s^{-1}. n is the dominant wavenumber after 300 days and c its propagation rate in m s^{-1}.

Identifier	U_0 (m s^{-1})	b ($\times 10^{-11}$ m^{-1} s^{-1})	n	c (m s^{-1})
U150b100N4	150	100	6	32.8
U150b050N4	150	50	5	49.3
U150b030N4	150	30	4	56.4
U150b020N4	150	20	3	61.6
U125b100N4	125	100	7	31.8
U125b050N4	125	50	6	41.1
U125b030N4	125	30	5	45.7
U125b020N4	125	20	4	50.7
U100b100N4	100	100	8	25.3
U100b050N4	100	50	7	31.3
U100b030N4	100	30	6	36.4
U100b020N4	100	20	5	39.4

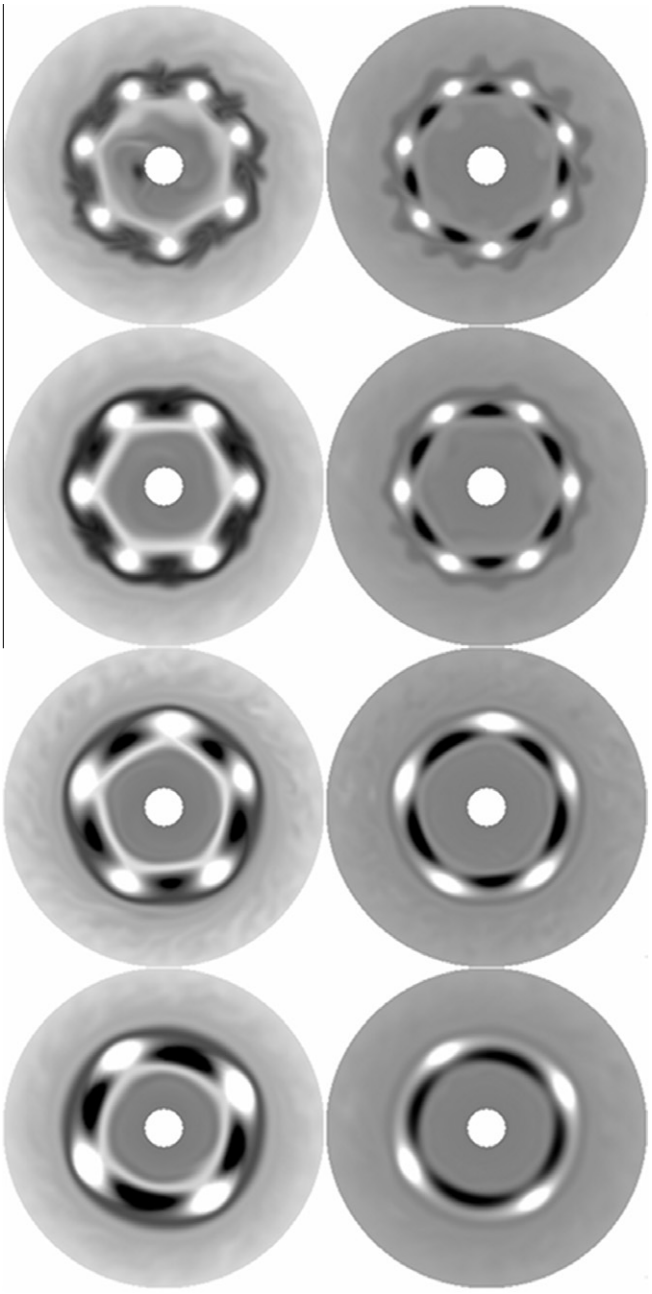

Fig. 3. Polar projections of potential vorticity at ≈200 mb (left) and ≈1500 mb (right) after 300 days, for simulations U125b100N4, U125b050N4, U125b030N4 , and U125b020N4 from top to bottom. The gray scale for the panels on the left goes from 8.5 to 10.5 PVU. The gray scale for the panels on the right goes from 0.3 to 0.5 PVU, which is the same scale used in Fig. 4 below. (PVU $\equiv 10^{-6}$ m^2 K s^{-1} kg^{-1}).

$$r(\varphi) = \frac{R_e^2 \cos(\varphi)}{\left[R_p^2 \sin^2(\varphi) + R_e^2 \cos^2(\varphi)\right]^{1/2}} \tag{4}$$

The meridional wavenumber is $k_y = 2\pi/\lambda_y$, where $\lambda_y = R(\varphi_0)\Delta\varphi$, and $\Delta\varphi$ is the width of the polygon that develops. As shown in the top panel of Fig. 4, $\Delta\varphi$ is different for different values of n. In our simulations, $\Delta\varphi \approx 5^\circ$ for $n = 4$, $\Delta\varphi \approx 4.5^\circ$ for $n = 5$, $\Delta\varphi \approx 4^\circ$ for $n = 6$, and $\Delta\varphi \approx 3.5^\circ$ for $n = 7$. This dependence of the propagation rate of the polygons following a Rossby wave dispersion relationship is similar to that observed for vortex streets in Jupiter (Morales-Juberías et al., 2002).

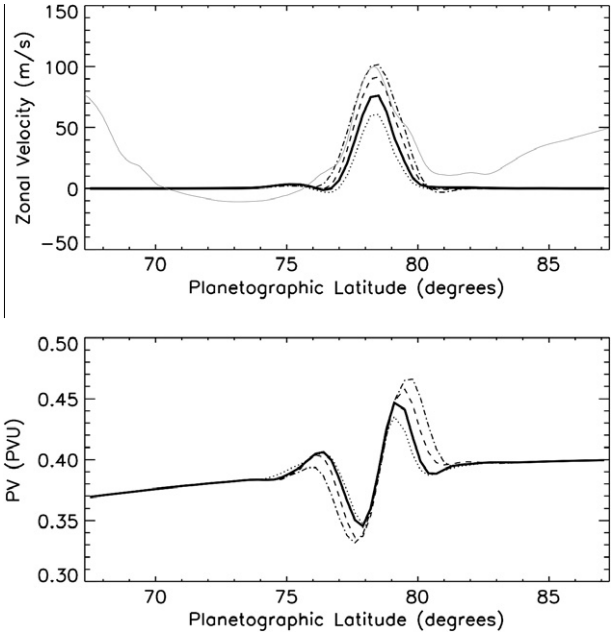

Fig. 4. Wind profiles (Top) and potential vorticity profiles (Bottom) at ≈1500 mb after 300 days for the simulations shown in Fig. 3. The dotted line corresponds to run U125b100N4 (heptagon), the continuous thick line to run U125b050N4 (Hexagon), the dashed line corresponds to run U125b030N4 (pentagon) and the dot-dashed line corresponds to U125b020N4 (square). The gray line in the top panel shows the zonal wind profile measured by Godfrey.

To check the numerical convergence of our results, we re-ran the case U125b050N4 doubling the grid resolution to be 512 × 128, which corresponds to a resolution of ≈170 × 170 km. The system equilibrated into the same wave number and propagation rate as those described above, which signals that our simulations are numerically converged.

In order to test the sensitivity of these results to the vertical stratification of the atmosphere (measured by the Brunt-Väisälä frequency at the bottom of the model), we varied the stratification of U125b050N4 to be $N = 0.005$, 0.006, and 0.007 s^{-1}. We find that the polygons' propagation speeds depend more strongly on its dominant wavenumber than on the tropospheric stratification. The cases U125b050N4 and U125b050N5 both take wavenumber 6 mode, and share a similar propagation speed of about 37 m s^{-1}, while they differ in stratification, $N = 0.004$ and 0.005 s^{-1}, respectively. The cases U125b050N6 and U125b050N7 both develop wavenumber 5 dominant modes, which propagate at ≈35 m s^{-1}, while they differ in stratification, $N = 0.006$ and 0.007 s^{-1}, respectively. Fig. 7 shows the longitudinal average of the zonal wind profile and of the potential vorticity at ≈1500 mb after 300 days for these simulations. Fig. 7 demonstrates that the equilibrated wind profiles continue to have reversals in the zonal mean PV profiles, which represent a violation of Charney-Stern stability criterion. The difference in PV outside the jet comes from the difference in the stratification. Fig. 8 shows how in these simulations, the flow also approaches neutral stability according to Arnol'd's second stability criterion.

As discussed earlier and shown in Table 1, the hexagonal mode of the case U150b100N4 does not reproduce the observed propagation rate of the saturnian Hexagon. The propagation rates of the polygons in our simulations follow the Rossby wave dispersion relationship (Fig. 6); thus, we attempted to control the propagation rate by varying Q_y in the initial condition. However, because the instabilities redistribute the momentum in nonlinear fashion in our simulations, controlling the value of Q_y in the final state with a polygonal formation proved to be a difficult challenge. We were

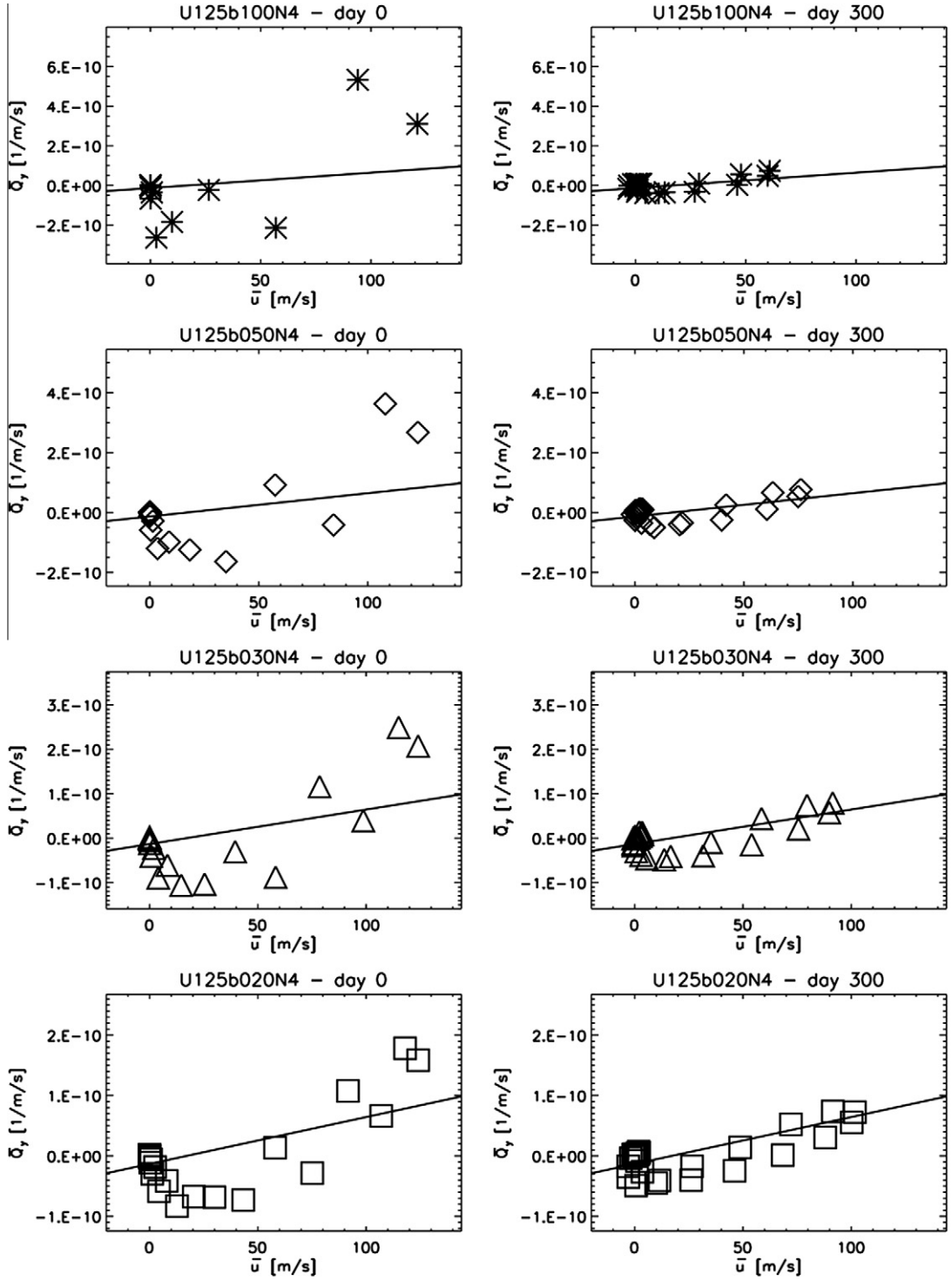

Fig. 5. Evolution of the meridional gradient of the zonal mean quasi-gesotrophic potential vorticity ($\overline{Q}_y$) versus mean zonal wind ($\bar{u}$) for the simulations shown in Fig. 3. The left panels show the initial condition and the right panels show day 300 for simulations U125b100N4 (asterisks), U125b050N4 (diamonds), U125b030N4 (triangles), and U125b020N4 (squares) from top to bottom. The solid line represents where $\overline{Q}_y = (\bar{u} - \alpha)/L_d^2$, where $\alpha = 17$ ms^{-1} and $L_d = 1135.31$ km for the center of the jet (Dowling and Read, 2010). (As in Fig. 6 the symbols on each panel represent the dominant wave number of the equilibrated flow.)

able to obtain quasi-stationary polygons when initializing the simulations with a zonal wind profile corresponding to case U125b100N4 modified by westward flows on each flank of the jet. For these simulations the initial wind profile is defined by:

$$U(\varphi) = U_0 \exp(-b\gamma^2(\varphi)/2U_0) - U_i\left[1 - \tanh\left(\frac{\ln^2(\varphi/\varphi_i)}{w_i^2}\right)\right];\ i = 1,2 \tag{5}$$

where summation over i is implied, U_i is the amplitude of the westward jets, φ_i is their central latitude, and w_i is a parameter that controls their width. In our simulations we placed these retrograde jets at $\varphi_1 = 79°$N and $\varphi_2 = 77.6°$N respectively, and fixed $w_1 = w_2$ to be 0.006. We ran cases with $U_1 = U_2 = 70$, 72.5, 75, 80 and 85 m s^{-1}, which led to polygons with dominant wavenumbers 5, 6, 6, 7, and 8, respectively, as listed in Table 2. As this parameter variation experiment demonstrates, the case with $U_1 = U_2 = 72.5$ m s^{-1} produced a

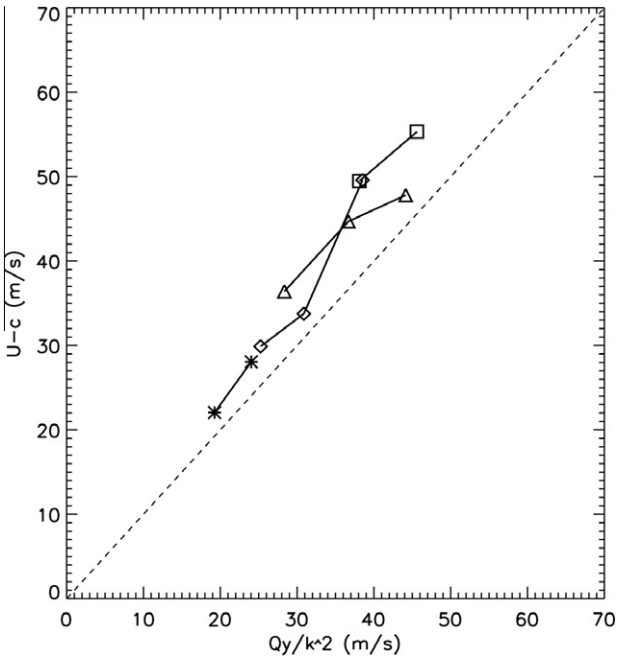

Fig. 6. Difference between the amplitude of the jet at 78.3 degrees and the phase speed of the polygon formed as a function of $Q_y/(k_x^2+k_y^2+k_d^2)$. All measurements correspond to the layer centered at ≈1500 mb after 300 days. Squares correspond to polygons with $n=4$, triangles represent polygons of $n=5$, diamonds represent polygons of $n=6$, and asterisks represent polygons of $n=7$.

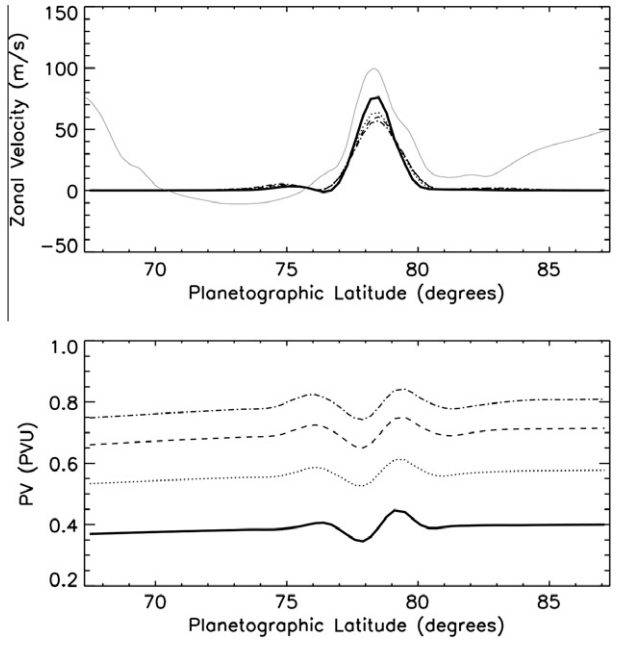

Fig. 7. Wind profiles (top) and potential vorticity profiles (bottom) at ≈1500 mb after 300 days simulated for the cases U125b050N4 (continuous thick line), U125b050N5 (dotted line), U125b050N6 (dashed line), and U125b050N7 (dot-dashed line).

Hexagon with a propagation speed of 0.7 m s^{-1}, which is within the uncertainty of the observed propagation rate of the Hexagon.

Fig. 9 shows the time evolution of the relative vorticity at the center of the jet for this simulation (H2 in Table 2). The figure shows that after ≈50 days, the dominant zonal wavenumber is six, and its propagation rate is ≈0.7 m s^{-1} as marked by the diagonal black line. Fig. 10 shows the polar projected maps of potential

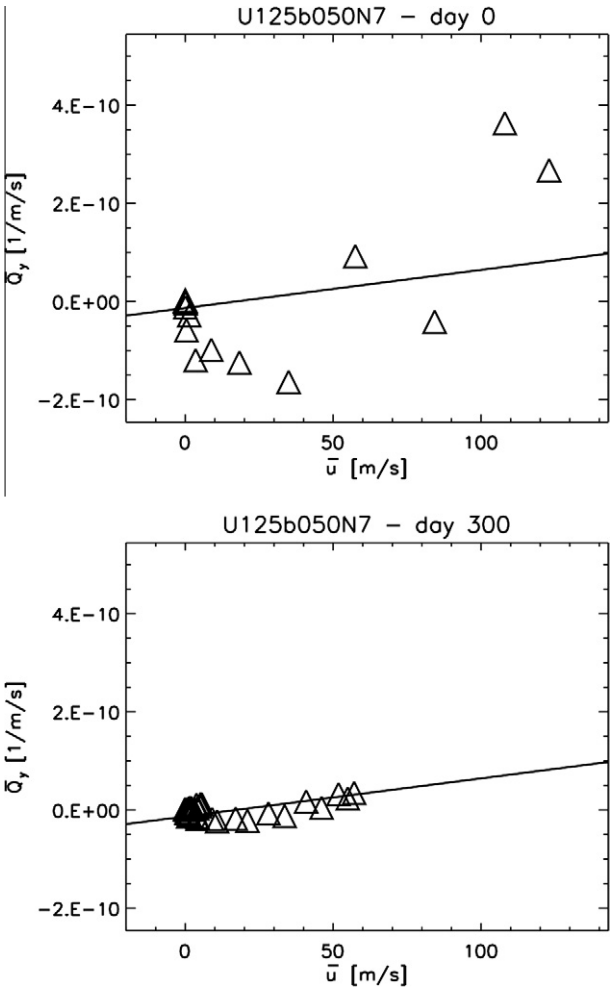

Fig. 8. Evolution of the meridional gradient of the zonal mean quasi-gesotrophic potential vorticity ($\overline{Q}_y$) versus mean zonal wind ($\bar{u}$) for simulation U125b050N7. The solid line represents where $\overline{Q}_y = (\bar{u}-\alpha)/L_d^2$, where $\alpha = 17$ ms^{-1} and $L_d = 1135.31$ km for the center of the jet (Dowling and Read, 2010).

Table 2
Results of the simulations initialized with zonal winds described by Eq. (5), and a thermal stratification in the bottom of the model of $N = 0.004$ s^{-1}. n is the dominant wavenumber after 300 days and c its propagation rate in m s^{-1}.

Identifier	U_1 (m s^{-1})	n	c (m s^{-1})
H1	70.0	5	0.9
H2	72.5	6	0.7
H3	75.0	6	−1.6
H4	80.0	7	−2.2
H5	85.0	8	−3.5

vorticity corresponding to this run, which show that the vortex street structure is much more pronounced than the nominal Gaussian-jet simulations shown in Fig. 3. Fig. 11 shows the average zonal wind profile and potential vorticity profile for this simulation after 300 days. Fig. 12 shows how in this simulation the flow also approaches neutral stability according to Arnol'd's second stability criterion.

In all our simulations, the zonal wind is initially constant in altitude, hence our initial condition is purely barotropic; however, as the simulations progress, a vertical shear that decays with height develops without forcing in all cases. The instabilities generate eddies and waves that redistribute momentum and kinetic energy in the system. This causes a broadening of the jet and a deceleration

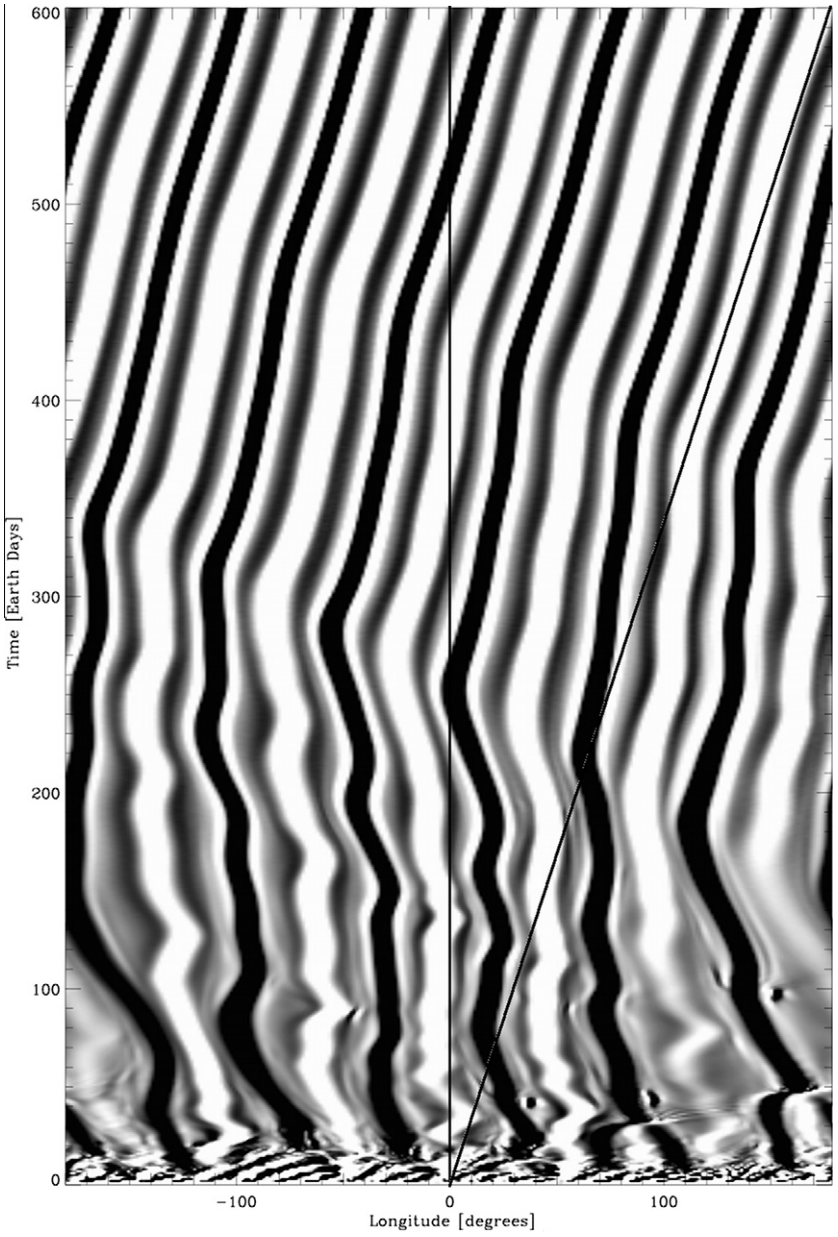

Fig. 9. Time-longitude map showing the evolution of the relative vorticity at the peak of the jet for 600 days for the simulation producing a quasi-stationary Hexagon. The black line going from 0 degrees at the beginning of the simulation (bottom of the figure) to 180 degrees at Earth-day 600 (top of the figure) marks the propagation rate of Saturn's Hexagon, which is of 0.8 ± 1.1 m s^{-1}.

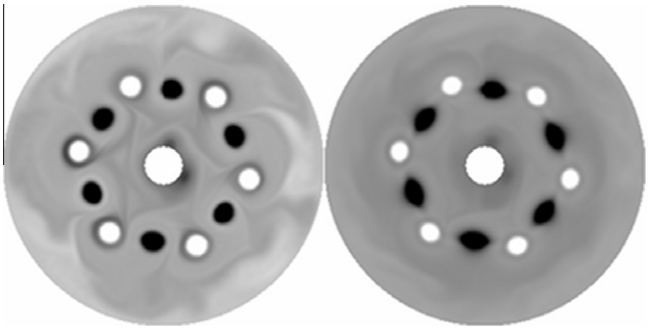

Fig. 10. Polar projections of potential vorticity at ≈200 mb (left) and ≈1500 mb (right) after 300 days for run H2. The gray scale for the panel on the left goes from 8.5 to 10.5 PVU. The gray scale for the panel on the right goes from 0.3 to 0.5 PVU. These are the same scales as in Fig. 3.

of its peak speed. This broadening and decelerating of the jet is characteristic of barotropic instabilities (Pedlosky, 1982). Fig. 13 shows the time evolution of four kinetic energy components (zonal barotropic, zonal baroclinic, eddy barotropic, and eddy baroclinic) for the case which develops a quasi-stationary Hexagon (H2 in Table 2), calculated following the scheme used by Sayanagi et al. (2010). As the eddy barotropic kinetic energy is much greater than both the eddy baroclinic and zonal baroclinic components, we identify barotropic instabilities as the dominant instability mode. The eddies that form on the flanks of the easward jet in this simulation are stronger than the eddies that form in the simulations initialized with simple Gaussian jets, and also stronger than those found by Godfrey's in the anticyclonic shear zone outside of Saturn's Hexagon. In this regard, our simulations are comparable to some laboratory experiments that show that the stability and coherence of the polygonal wave pattern is a manifestation of

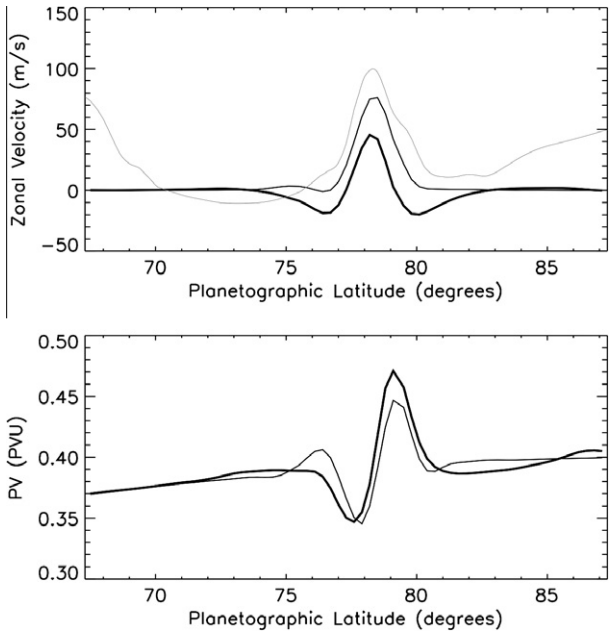

Fig. 11. The thick black line in the panels shows the wind profiles (top) and potential vorticity profiles (bottom) at ≈1500 mb after 300 days for the simulations H2 which produces a quasi-stationary Hexagon. The thin black line corresponds to the run U125b050N4, which produces a fast propagating Hexagon. The thin continuous gray line corresponds to the profile measured by Godfrey.

the vortex street structure (Niino and Misawa, 1984; Marcus and Lee, 1998; Barbosa-Aguiar et al., 2010).

3. Discussion and conclusions

At the high latitude of the Hexagon, the beta parameter ($\beta = df/dy$, where $f = 2\Omega\sin(\varphi)$ is the Coriolis parameter) is very small compared to the second derivative of the mean zonal wind, and the necessary Rayleigh–Kuo criterion for barotropic stability is easily violated (Ingersoll and Pollard, 1982; Read et al., 2009a). Though violation of this criterion does not ensure that an instability will be produced, Barbosa-Aguiar et al. (2010) expanded the barotropic stability analysis into cases with finite deformation radius and estimated that planetary wavenumber 6 becomes the most unstable mode when the deformation radius is 2500 km. They also performed a series of rotating tank experiments with which they show how long-lived polygonal structures resembling Saturn's north polar Hexagon can be caused by the nonlinear equilibration of barotropically unstable zonal jets. The Gaussian jets adopted in our simulations violate the Rayleigh–Kuo criterion, and past linear stability analyses demonstrate that barotropic instabilities indeed arise in such a profile (Holland and Haidvogel, 1980).

We explore the nonlinear dynamical regimes of the instabilities beyond what has been analyzed through the aforementioned linear studies. Our nonlinear simulations demonstrate that instabilities initially grow exponentially as predicted by linear analysis; however, when their amplitudes reach large enough for the nonlinear effects to be important, the instabilities saturate at a constant amplitude as shown in Fig. 13. When the instabilities saturate, stable polygonal structures emerge, and a dominant wavenumber 6 or "hexagon" is among the stable solutions produced by our simulations.

We further show that the propagation rate of the polygon can be modified by adding westward flows to the flanks of the eastward Gaussian jet core. By adding these westward flows to the zonal wind profile, the initial shear in the flanks of the eastward jet is

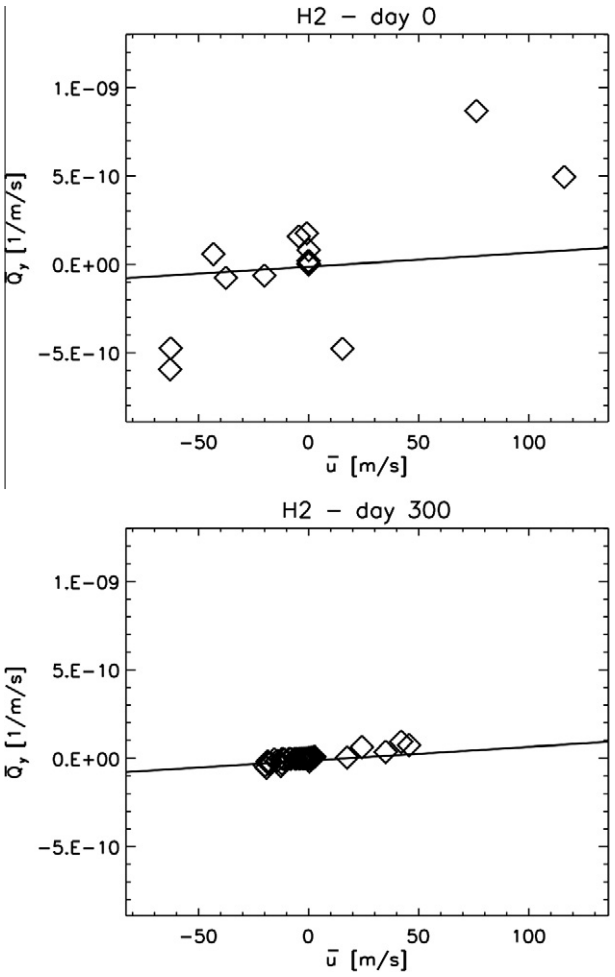

Fig. 12. Evolution of the meridional gradient of the zonal mean quasi-gesotrophic potential vorticity ($\overline{Q}_y$) versus mean zonal wind ($\bar{u}$) for the simulation shown in Fig. 10. The top panel shows the initial condition and the bottom panel shows day 300 for this simulation. The solid line represents where $\overline{Q}_y = (\bar{u} - \alpha)/L_d^2$, where $\alpha = 17\ \mathrm{ms}^{-1}$ and $L_d = 1135.31$ km for the center of the jet (Dowling and Read, 2010). (As in Fig. 6 the symbols on each panel represent the dominant wave number of the equilibrated flow.)

stronger than in the cases shown in Table 1. Thus the spots that form on the flanks of the main eastward jet have higher vorticities, and the amplitude of the zonal wind in their location is smaller than in the simple Gaussian-jet case. Barbosa-Aguiar's (2010) experimental setup did not allow investigations of the factors that control the Hexagon's propagation rate. The Hexagon is stationary only with respect to the commonly accepted Voyager System III rotation rate (Ω_{III} frame). We note that the internal rotation rate of Saturn is not well-constrained (Kurth et al., 2008; Helled et al., 2009; Read et al., 2009b), and thus the phase speed of Saturn's Hexagon with respect to the planet's bulk (interior) rotation remains an important open question.

Flierl et al. (1987) studied the nonlinear evolution of barotropic beta plane jets as a function of the beta parameter and the dominant wavenumber. Within this space of parameters, they showed how the jets can equilibrate forming a stable vortex street or a steady meander. In our Hexagon experiments the value of beta is well-constrained by the feature's latitude, and our goal is to reproduce the wavenumber 6 structure and its observed propagation rate. Our simulations demonstrate that a stable hexagonal structure with a propagation rate consistent with observation can be produced by a vortex street that emerges from the equilibration of a shear-unstable jet; however, Cassini observations do not show

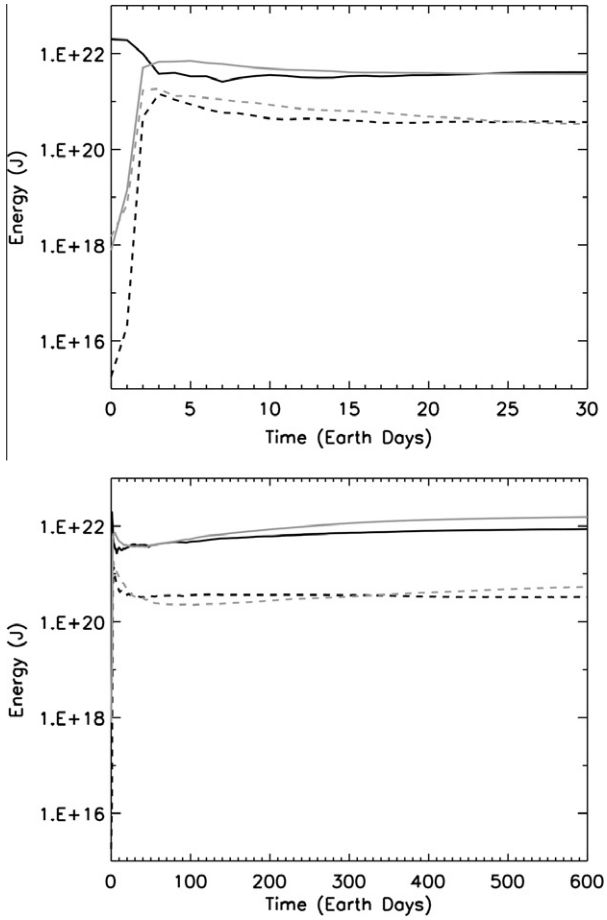

Fig. 13. Time evolution of the kinetic energy components for the run H2. The solid lines represent the barotropic components of zonal (black) and eddy (gray) kinetic energy. The dashed lines represent the baroclinic components of zonal (black) and eddy (gray) kinetic energy. The top panel shows only the first 30 days of the simulation. The bottom panel shows 600 days in the same simulation.

large vortices that must exist if the Hexagon were indeed a feature associated with a vortex street. Thus, to find a scenario in which a hexagonal feature could form out of a steadily meandering jet, we have tested a variety of initial wind profiles and forcing schemes.

First, approaching the problem as an initial value problem (i.e. not using forcing), we ran several simulations initializing the model with zonal winds like those described by Eqs. (1) and (5) that had different initial vertical shear profiles. In some simulations we tried hyperbolic and Gaussian vertical wind profiles similar to those used by Williams (1996, 1997) for Jupiter studies. In others we used simple linear increasing and decreasing profiles like those described by Morales-Juberías et al. (2003). In all of these simulations, the dominant wavenumber that develops, and its propagation rate are affected by the shape of the vertical shear of the zonal winds. Nonetheless, they all equilibrated into a vortex street, not a steady meandering.

Second, we explored the effect of different forcing terms on the equilibration of the jet. Recent infrared Cassini observations reveal the presence of a darker Hexagon located equatorward (southward) of the brighter Hexagon identified with that observed in the Voyager era. The clouds of this darker Hexagon are higher (2.5–3.0 bars) than the clouds in the brighter Hexagon (3.5 bars) which could be due to a difference in the cloud properties between the cyclonic and anticyclonic regions of the jet in which the Hexagon is centered (Baines et al., 2009). Gierasch et al. (1973) showed how large horizontal scale radiative thermal forcing can lead to large scale dynamical instabilities. The spatial and temporal scales of such instabilities are poorly constrained by current observations, which makes construction of a unique parameterization impossible. We ran a series of simulations applying different horizontal thermal forcing terms to the jet. In all cases the instabilities did not saturate into a stable configuration.

Finally, it is also possible that the excitation from large eddies in the thermally-convecting layers beneath the outermost stratified layers is needed to drive the instability in the observed meandering regime (McIntyre, 2008). From observations of the southern hemisphere Del Genio et al. (2007) concluded that the eddies add momentum to the eastward jets and remove momentum from the westward jets. Over time this kind of forcing could drive the final wind profile in Fig. 11 closer to the observed profile.

In summary, our simulations demonstrate that a stable hexagonal flow can emerge when a barotropically unstable zonal jet nonlinearly equilibrates, which is in agreement with the laboratory experiment by Barbosa-Aguiar et al. (2010), and like the laboratory counterpart, the hexagonal structure that emerges in our simulations is a vortex street. However, the lack of large vortices in the Hexagon region of Saturn does not appear consistent with a vortex street model. In addition, our simulations suggest that for a vortex street model to reproduce the observed propagation rate of the Hexagon, the 78°N jet's speed must deviate beyond the uncertainties in the measurements by Godfrey (1988). Based on these results, we propose that a steadily meandering jet, which does not require the existence of large vortices adjacent to the Hexagon, may be an alternative explanation and one that could guide a future simulation study.

Acknowledgments

We acknowledge Tim Mattox for his help with the setup of the parallel cluster RAVEN on which some of these simulations were carried out. Computational resources were also provided by the New Mexico Computing Applications Center and New Mexico Institute of Mining and Technology. This work was supported by NASA Planetary Atmospheres Grant numbers NNX08AE91G (NMT), NNG05GO06Gd and NNX08AE64G (UofL).

References

Allison, M., Godfrey, D.A., Beebe, R.F., 1990. A wave dynamical interpretation of Saturn's polar Hexagon. Science 247 (March), 1061–1063.

Baines, K.H., Momary, T.W., Fletcher, L.N., Showman, A.P., Roos-Serote, M., Brown, R.H., Buratti, B.J., Clark, R.N., Nicholson, P.D., 2009. Saturn's north polar Cyclone and Hexagon at depth revealed by Cassini/VIMS. Planet. Space Sci. 57 (December), 1671–1681.

Barbosa-Aguiar, A.C., Read, Peter L., Wordsworth, Robin D., Salter, T., Hiro-Yamazaki, Y., 2010. A laboratory model of Saturn's north polar Hexagon. Icarus 206 (2), 755–763. ISSN 0019-1035.

Caldwell, J., Hua, X.-M., Turgeon, B., Westphal, J.A., Barnet, C.D., 1993. The drift of Saturn's north polar spot observed by the Hubble Space Telescope. Science 260 (April), 326–329.

Del Genio, A.D., Barbara, J.M., Ferrier, J., Ingersoll, A.P., West, R.A., Vasavada, A.R., Spitale, J., Porco, C.C., 2007. Saturn eddy momentum fluxes and convection: First estimates from Cassini images. Icarus 189 (August), 479–492.

Desch, M.D., Kaiser, M.L., 1981. Voyager measurement of the rotation period of Saturn's magnetic field. Geophys. Res. Lett. 8 (March), 253–256.

Dowling, T.E., 1995. Estimate of Jupiter's deep zonal-wind profile from Shoemaker-Levy 9 data and Arnol'd's second stability criterion. Icarus 117 (October), 439–442.

Dowling, T.E., Read, P.L. 2010. Estimate of Saturn's deep zonal-wind profile. Icarus, submitted for publication.

Dowling, T.E., Fischer, A.S., Gierasch, P.J., Harrington, J., Lebeau, R.P., Santori, C.M., 1998. The Explicit Planetary Isentropic-Coordinate (EPIC) atmospheric model. Icarus 132 (April), 221–238.

Flierl, G.R., Malanotte-Rizzoli, P., Zabusky, N.J., 1987. Nonlinear waves and coherent vortex structures in barotropic β-plane jets. J. Phys. Oceanogr. 17 (September), 1408–1438.

Gierasch, P.J., Ingersoll, A.P., Williams, R.T., 1973. Radiative instability of a cloudy planetary atmosphere. Icarus 19 (August), 473–481.

Godfrey, D.A., 1988. A hexagonal feature around Saturn's North Pole. Icarus 76 (November), 335–356.
Helled, R., Schubert, G., Anderson, J.D., 2009. Jupiter and Saturn rotation periods. Planet. Space Sci. 57 (October), 1467–1473.
Holland, W., Haidvogel, D.B., 1980. A parameter study of the mixed instability of idealized ocean currents. Dynam. Atmos. Oceans 4 (February), 185–215.
Humphreys, T., Marcus, P.S., 2007. Vortex street dynamics: The selection mechanism for the areas and locations of Jupiter's vortices. J. Atmos. Sci. 64, 1318–1333.
Ingersoll, A.P., Pollard, D., 1982. Motion in the interiors and atmospheres of Jupiter and Saturn – Scale analysis, anelastic equations, barotropic stability criterion. Icarus 52 (October), 62–80.
Jansson, T.R.N., Haspang, M.P., Jensen, K.H., Hersen, P., Bohr, T., 2006. Polygons on a rotating fluid surface. Phys. Rev. Lett. 96 (17), 174502-1–174502-4.
Kurth, W.S., Averkamp, T.F., Gurnett, D.A., Groene, J.B., Lecacheux, A., 2008. An update to a saturnian longitude system based on kilometric radio emissions. J. Geophys. Res. (Space Physics) 113. A05222-1—A05222-10.
Lebeau, R.P., Dowling, T.E., 1998. EPIC simulations of time-dependent, three-dimensional vortices with application to Neptune's great dark spot. Icarus 132 (April), 239–265.
Marcus, P.S., Lee, C., 1998. A model for eastward and westward jets in laboratory experiments and planetary atmospheres. Phys. Fluids 10 (June), 1474–1489.
McIntyre, M.E., 2008. Potential-vorticity inversion and the wave-turbulence jigsaw: Some recent clarifications. Adv. Geosci. 15 (June), 47–56.
Morales-Juberías, R., Sánchez-Lavega, A., Lecacheux, J., Colas, F., 2002. A comparative study of jovian anticyclone properties from a six-year (1994–2000) survey. Icarus 157 (May), 76–90.
Morales-Juberías, R., Sánchez-Lavega, A., Dowling, T.E., 2003. EPIC simulations of the merger of Jupiter's White Ovals BE and FA: altitude-dependent behavior. Icarus 166 (November), 63–74.
Niino, H., Misawa, N., 1984. An experimental and theoretical study of barotropic instability. J. Atmos. Sci. 41 (June), 1992–2011.
Pedlosky, J., 1982. Geophysical Fluid Dynamics. Springer-Verlag, New York and Berlin. 636p.
Read, P.L., Conrath, B.J., Fletcher, L.N., Gierasch, P.J., Simon-Miller, A.A., Zuchowski, L.C., 2009a. Mapping potential vorticity dynamics on Saturn: Zonal mean circulation from Cassini and Voyager data. Planet. Space Sci. 57 (December), 1682–1698.
Read, P.L., Dowling, T.E., Schubert, G., 2009b. Saturn's rotation period from its atmospheric planetary-wave configuration. Nature 460 (July), 608–610.
Sanchez-Lavega, A., Lecacheux, J., Colas, F., Laques, P., 1993. Ground-based observations of Saturn's north polar spot and Hexagon. Science 260 (April), 329–332.
Sayanagi, K.M., Ewald, S.P., Ingersoll, A.P., 2009. New Cassini ISS Observations of Saturn's Northern Hemisphere Ribbon and Hexagon. In: AAS/Division for Planetary Sciences Meeting Abstracts, volume 41 of AAS/Division for Planetary Sciences Meeting Abstracts, page 10.08, September.
Sayanagi, K.M., Morales-Juberías, R., Ingersoll, A.P., 2010. Saturn's Northern Hemisphere Ribbon: Simulations and comparison with the meandering Gulf stream. J. Atmos. Sci. 67 (August), 2658–2678.
Sommeria, J., Meyers, S.D., Swinney, H.L., 1989. Laboratory model of a planetary eastward jet. Nature 337 (January), 58–61.
Tyler, G.L., Eshleman, V.R., Anderson, J.D., Levy, G.S., Lindal, G.F., Wood, G.E., Croft, T.A., 1982. Radio science with Voyager 2 at Saturn – Atmosphere and ionosphere and the masses of Mimas, Tethys, and Iapetus. Science 215 (January), 553–558.
Vatistas, G.H., 1990. A note on liquid vortex sloshing and Kelvin's equilibria. J. Fluid Mech. 217, 241–248.
Vatistas, G.H., Wang, J., Lin, S., 1994. Recent findings on Kelvin's equilibria. Acta Mech. 103, 89–102.
Williams, G.P., 1996. Jovian dynamics. Part 1: Vortex stability, structure, and genesis. J. Atmos. Sci. 53 (September), 2685–2734.
Williams, G.P., 1997. Planetary vortices and Jupiter's vertical structure. J. Geophys. Res. 102, 9303–9308.